

Numerical simulations of transition and long-term response of a wind turbine airfoil

T. C. L. Fava¹, N. Sørensen², D. S. Henningson¹ and A. Hanifi¹

¹FLOW, Department of Engineering Mechanics, KTH Royal Institute of Technology, SE-100 44 Stockholm, Sweden

²Department of Wind Energy, Technical University of Denmark, Risø Campus, Roskilde, Denmark

Numerical simulations of a wind turbine airfoil of the FFA-W3 series corresponding to a section of the DTU 10-MW Reference Wind Turbine are performed. Wall-resolved large eddy simulations (LES) are carried out with the solvers NEK5000 and ELLIPSYS for a chord Reynolds number of 1×10^5 and effective angle of attack $AoA = 3.1^\circ - 3.3^\circ$. It is shown that a domain width of 10% of the chord is enough to capture the evolution of the main disturbances besides reproducing well the time-averaged flow. ELLIPSYS is validated against NEK5000 for LES, indicating close results for the mean flow and most amplified perturbations. ELLIPSYS underpredicts the amplitude of Tollmien-Schlichting waves in the attached boundary layer due to a higher numerical dissipation but closely predicts the evolution of the Kelvin-Helmholtz (KH) mode in the laminar separation bubble. The latter is in close agreement with the predictions from parabolized stability equations (PSE). The shape of the mode is obtained with spectral proper orthogonal decomposition (SPOD), clearly showing the wavepacket of the KH mode forming in the LSB. The long-term evolution of the flow is computed with ELLIPSYS. A slow modulation of the normal force coefficient is identified with an amplitude of 10.5% and a period of 48 flowthroughs, or equivalently a frequency $f = f^*c/U_\infty = 0.021$ and Strouhal number $St = f \sin AoA = 0.0012$. This frequency corresponds to low-frequency oscillations (LFOs) observed in several airfoil studies. However, St is lower than previously noticed and occurs at a smaller AoA . In the DTU 10-MW Reference Wind Turbine, the period of these oscillations corresponds to 7.7 blade rotations. The periodic stalling and unstalling of the flow could trigger the LFO. The reverse flow on both sides of the airfoil is high enough to allow absolute instability, which may be responsible for the periodic bubble bursting.

1. Introduction

Flow separation often affects wind turbine blades due to elevated flow incidence angles and thick airfoils (Corten 2001). Raju *et al.* (2008) observed at least three main natural frequencies $f = f^*c/U_\infty$ (f^* , U_∞ , and c are the dimensional temporal frequency, free-stream velocity, and chord length, respectively) in airfoils with separation due to wake shedding ($f = O(1)$), Kelvin-Helmholtz modes ($f = O(10)$), and separation shedding ($f = O(1)$). A separated shear layer over an airfoil is highly unstable, allowing the appearance of inviscid Kelvin-Helmholtz (KH) modes (Dovgal *et al.* 1994). The central frequency of unstable KH modes typically determines the mean vortex shedding frequency $f_s \theta_s / u_s = 0.005 - 0.016$, where θ_s

and u_s are the momentum thickness and edge velocity at the separation point (Pauley *et al.* 1990; Brinkerhoff & Yaras 2011).

The LSB may develop flapping, defined as the intermittent global motion of the separated shear layer upon separation (Jaroslowski *et al.* 2023). This motion displays low frequencies, 100 times lower than the primary KH instability, i.e., $f = O(10^{-1})$ (Zaman *et al.* 1989; Rist & Maucher 2002). Rist (2003) put forward three possible mechanisms for flapping. The first involves an LSB resonance to long-wavelength disturbances. The occurrence of absolute instability (Huerre & Monkewitz 1990), which may cause such an oscillatory behavior, requires a minimum reverse flow of 12% – 25% (Hammond & Redekopp 1998; Alam & Sandham 2000; Rist & Maucher 2002; Fasel & Postl 2004; Diwan & Ramesh 2009; Rodríguez *et al.* 2013) and the inflection point in the streamwise velocity profile to be located below the zero mass-flux line, i.e., $y_i < y_b$ (Avanci *et al.* 2019). The second considers a growth-decay mechanism (Cherry *et al.* 1984; Dovgal *et al.* 1994), consisting of several steps. Firstly, an incoming disturbance increase leads the LSB to shrink. The new, smaller LSB is less unstable, and disturbances are less amplified, allowing the LSB to enlarge over time. Eventually, the LSB grows big enough, shifting transition upstream and restarting the cycle. The third possibility is the interaction of the flow with the far-field boundaries or trailing edge noise (Arbey & Bataille 1983; Nash *et al.* 1999; McAlpine *et al.* 1999; Desquesnes *et al.* 2007; Deng *et al.* 2007). The frequency of the oscillations generated by resonance with the boundaries depends on the domain size, and the frequency of those generated by trailing-edge noise is of the order of the inverse of the flowthrough time. Ehrenstein & Gallaire (2008) found that the superposition of global modes, whose structures start inside the LSB and extend beyond the reattachment point, gives rise to an alternate cancellation yielding a low-frequency beating characteristic of flapping. The work of Cherubini *et al.* (2010), in which the role of the non-normality of these modes in the occurrence of flapping was highlighted, agrees with those results. Furthermore, the experimental study by Passaggia *et al.* (2012) of the separated flow behind a bump identified the global modes predicted by Ehrenstein & Gallaire (2008), whose structure presented a spanwise oscillation.

Low-frequency oscillations (LFO) characterized by strong lift variations have been identified experimentally in several studies (Jones 1933; Farren 1935; Armstrong & Stevenson 1960; Moss 1979; Zaman *et al.* 1987; Zaman & Potapczuk 1989; Bragg *et al.* 1993; Heinrich 1994; Broeren 2000; Gurbacki 2003; Rinoie & Takemura 2004; Tanaka 2004; Almutairi & AlQadi 2013). These oscillations typically have a Strouhal number in the range $St = (f^*c/U_\infty) \sin AoA = 0.0048 - 0.03$ (Ansell & Bragg 2015), where AoA is the angle of attack. The frequency of these oscillations is in the range of flapping, but the amplitude of the variations is much larger than that produced by the latter, suggesting another mechanism (Bragg *et al.* 1996). In the experimental and numerical study of Zaman *et al.* (1989), the lift coefficient fluctuations reached 50% of the mean value of this variable for an airfoil at $AoA = 15^\circ$. Commensurate lift variations also occurred in the experimental work of Bernardini *et al.* (2016), considering a NACA 64₃-618 airfoil. Furthermore, Zaman *et al.* (1989) found that these oscillations are hydrodynamic, with a phase speed $c_p = c_p^*/U_\infty = 0.7$ and $St = 0.02$. This frequency agrees with the results from Farren (1935) and Zaman *et al.* (1987), and it is one order lower than bluff-body shedding, which occurred for a deep-stall condition at $AoA = 22.5^\circ$, with $c_p = 0.95$ and $St = 0.3$. The frequency $St = 0.02$ is also one order lower than that of trailing-edge noise (Brooks & Schlinker 1983; Jones *et al.* 2010). The phase speed of the low-frequency mode obtained by Zaman *et al.* (1989) is much higher than that computed by Ansell & Bragg (2015) ($c_p = 0.145$) and Crimi (1974) ($c_p = 0.25$), suggesting a large variability in the LFO modes. The low-frequency mechanism was attributed to the periodic stalling and unstalling of the flow on the suction side (Zaman *et al.* 1989; Broeren & Bragg 1999; Sandham 2008). The maximum lift phase corresponds

to a state with the longest LSB on the suction side. As time progresses, the pressure gradient flattens out, and the flow eventually becomes fully stalled. However, this reduces the adverse pressure gradient (APG), which allows the flow to reattach to form an LSB. The APG gradually increases again, and the reattachment point progressively moves downstream until the flow is totally separated again, restarting the cycle. Notice that the process where the LSB becomes a region of fully stalled flow is denominated bursting (Gaster 1967). Some works have associated bursting with the inception of absolute instability (Almutairi & AlQadi 2013; Negi *et al.* 2018). Nevertheless, LFO is essentially a two-dimensional phenomenon, unlike cases with three-dimensional stall cells (Broeren & Bragg 2001; Sandham 2008). Notice that the described cycle can be captured with simple models, which contain the interaction between the boundary layer and potential flow (Sandham 2008). However, in order to capture correct frequencies, it seems that at least an LES approach is necessary (Almutairi & AlQadi 2013). LFO has only been observed in airfoils with a thin-airfoil stall or a combination of thin-airfoil and trailing-edge stalls (Ansell & Bragg 2015). Thin-airfoil stall happens when the flow separates due to an APG but reattaches owing to transition, forming a separation bubble (Almutairi & AlQadi 2013). Sufficiently high Reynolds numbers would act to reduce thin-airfoil stall and, consequently, LFO. This phenomenon has been observed for Re_c as high as $(1.0 - 5.8) \times 10^6$ (McCullough & Gault 1951; Bragg *et al.* 1996; Hristov & Ansell 2018; Liu & Xiao 2020). Bernardini *et al.* (2016) showed that LFO may occur even in the post-stall regime and be triggered or suppressed with acoustic active control.

More recently, Tang *et al.* (2021) showed that merging shedding vortices could also generate a low-frequency oscillation of the order of previously observed LFO in airfoils. Bouchard *et al.* (2022) found that the LFO on a stalled airfoil could be traced back to the upstream propagation inside the separated flow of relatively high-frequency ($St \approx 3$) perturbations generated at the trailing edge up to the leading edge, exciting low-frequency perturbations with $St = 0.02$. Aniffa & Mandal (2023) showed the occurrence of LFO on a flat plate with separated flow for high APG, where the shedding of vortices from the shear layer displayed an intermittent behavior. LFO was not significant for low APG. Further recent studies of LFO on an airfoil include Eljack & Soria (2020) and Eljack *et al.* (2021), which provided detailed accounts of the pre-stall and post-stall behaviors of this phenomenon. Recent wall-resolved simulations of rotating wind-turbine blade sections have further shown that rotation can modify the transition scenario by changing the amplification of Tollmien–Schlichting, Kelvin–Helmholtz and crossflow-type disturbances in the laminar separation bubble (Fava *et al.* 2024b). These results highlight the sensitivity of transition mechanisms on wind-turbine sections to rotation, Reynolds number and separation-bubble dynamics.

The current work studies transition and low-frequency oscillations on a thick wind turbine airfoil at $Re_c = 1 \times 10^5$ with wall-resolved (no subgrid-scale model) large eddy simulations (LES). For that, the incompressible Navier–Stokes solver ELLIPSYS, which is less computationally demanding than Nek5000, is validated against the latter and employed for the long-time integration of the equations. Linear stability analysis is used to assess the boundary layer stability. The paper is divided as follows: §2 presents the airfoil geometry, modeling equations, flow solvers, and grid quality assessment. §3 shows the study of the dependence of the results on the domain spanwise width. §4 exhibits the validation results of ELLIPSYS. §5 presents the study of the long-term variation of the lift coefficient. Finally, §6 displays the conclusions of this work.

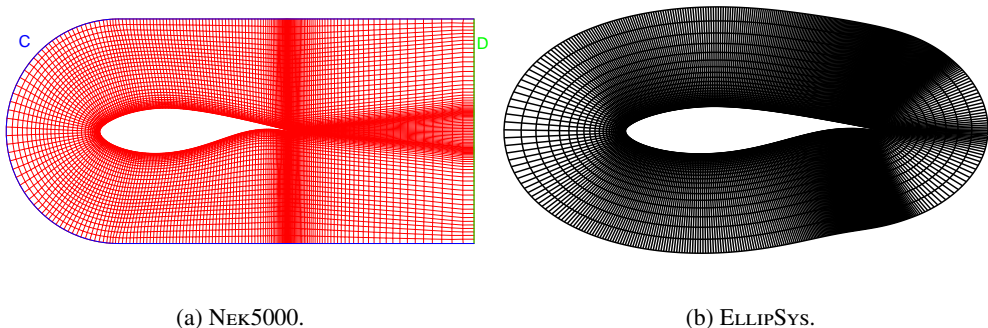


Figure 1: Computational domains and meshes employed in the simulations. Only the elements (without the Gauss-Lobatto-Legendre points) are shown in the NEK5000 grid for enhanced visibility. In the ELLIPSYS grid, every third cell in each direction is exhibited.

2. Methods

2.1. Problem modeling

A blade section at 68% of the radius of the DTU 10-MW Reference Wind Turbine (Bak *et al.* 2012) with a spanwise width of 10% of the chord at a Reynolds number $Re_c = 1 \times 10^5$ is studied. The airfoil is a blend of 96% of the FFA-W3-241 and 4% of the FFA-W3-301 profiles (Björck 1990). The employed profile and computational domains in the simulations with the codes NEK5000 and ELLIPSYS can be observed in Fig. 1.

The equations modeling the problem are the incompressible Navier–Stokes equations given by

$$\begin{aligned} \nabla \cdot \mathbf{u} &= 0, \\ \frac{\partial \mathbf{u}}{\partial t} + \mathbf{u} \cdot \nabla \mathbf{u} &= -\nabla p + \frac{1}{Re_c} \nabla^2 \mathbf{u}, \end{aligned} \quad (2.1)$$

where $\mathbf{u} = (u_x, u_y, u_z)$, p is the pressure, $Re_c = U_\infty c / \nu$ is the chord-based Reynolds number, U_∞ is the relative free-stream inflow velocity, c is the chord length, and ν is the kinematic viscosity. All quantities are non-dimensionalized by U_∞ and c if not otherwise stated. Although it is assumed that the flow arrives with an angle of attack $AoA = \arctan\left(\frac{V_\infty}{\Omega r}\right) = 1.2^\circ$, where V_∞ is the wind speed, Ω is the rotation rate, and r is the radial location, rotation effects are not taken into account. Notice that the relative velocity can also be written as $U_\infty = \sqrt{V_\infty^2 + (\Omega r)^2}$.

As Dirichlet boundary condition for solving system 2.1, \mathbf{u} is specified at the inlet boundary, defined as surface C in Fig. 1a (equivalently for ELLIPSYS). This boundary condition was obtained with Reynolds-Averaged Navier–Stokes (RANS) simulations carried out with ELLIPSYS (in RANS mode), whose results were interpolated on the boundaries of both NEK5000 and ELLIPSYS computational domains. Moreover, a Neumann boundary condition of the form $[-p\mathbf{I} + 1/Re_c \nabla \mathbf{u}] \cdot \mathbf{n} = 0$, where \mathbf{I} is the identity matrix and \mathbf{n} is the outward-oriented normal unitary vector, is applied to the outlet plane (surface D in Fig. 1a). Finally, periodicity boundary conditions are applied in the spanwise direction.

2.2. Numerical methods

The implicit large eddy simulations (LES) approach is taken, in which the incompressible Navier–Stokes equations (Eq. 2.1) are solved without any turbulence model. Part of the simulations is performed with NEK5000 (Fischer *et al.* 2008), which is an open-source, highly scalable, and portable code based on the spectral element method (SEM), offering minimal dissipation and numerical noise, high accuracy, and nearly exponential convergence with the polynomial order N . SEM (Patera 1984) can be considered a high-order extension of the finite element method (FEM). SEM discretizes the computational domain into a finite number of non-overlapping elements. The basis functions, defined on each element, are Lagrange polynomials of order N . Here, $N = 7$ was employed, providing converged results as shown in Fava *et al.* (2024a). The equations are solved in weak form using the $\mathbb{P}_N - \mathbb{P}_{N-2}$ formulation, in which the velocity is expanded on Gauss–Lobatto–Legendre (GLL) points and the pressure on Gauss–Legendre (GL) points (Deville *et al.* 2002). Third-order implicit backward differentiation (BDF), with an extrapolation scheme of order three for the convective term, is employed for time integration. The Courant number has been carefully assessed and is always below 0.3, corresponding to a fixed $\Delta t = 5 \times 10^{-6}$ based on U_∞ and c . Since SEM is characterized by very low numerical dissipation, which could lead to numerical instabilities, the highest 33% of wavenumbers are filtered with an implicit filter that preserves the zero divergence of the flow (Negi *et al.* 2017). The filter amplitude is very low and corresponds to 2×10^{-7} in an explicit filter.

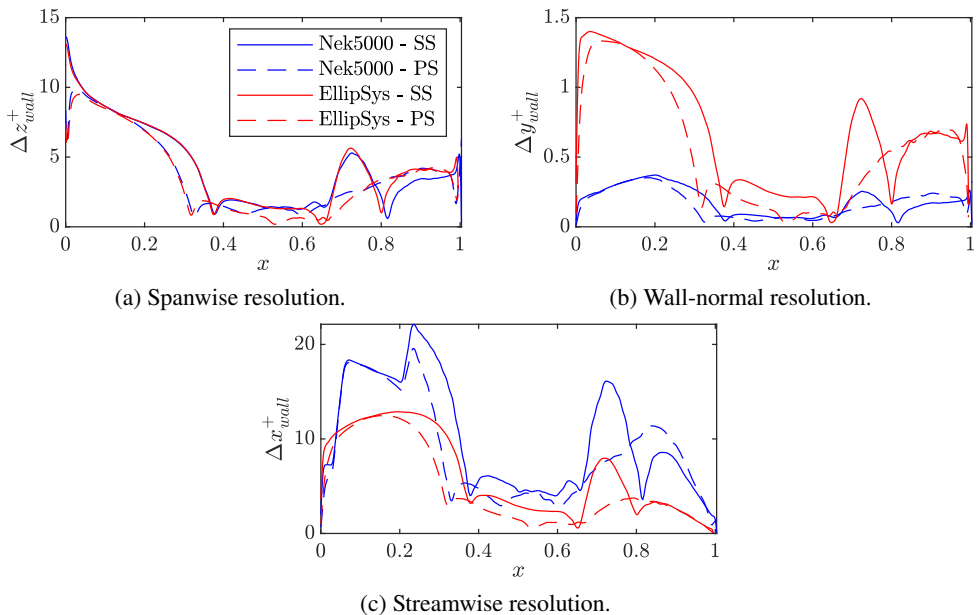
The computations also employed ELLIPSYS, a general-purpose 3D solver developed at DTU/Risø (Michelsen 1992, 1994; Sørensen 1994). The code solves the incompressible Navier–Stokes equations in curvilinear coordinates, using block-structured, finite volume discretization. The formulation involves primitive variables (pressure-velocity) in a collocated grid. The SIMPLE algorithm is used to solve the pressure correction, with pressure (odd/even) decoupling being avoided using Rhie/Chow interpolation. The convective terms are discretized with a second-order upwind scheme, whereas a central scheme is employed for the viscous ones. The equations are integrated in time using a second-order iterative time-stepping (dual time-stepping), where the equations are resolved iteratively with under-relaxation within each time step. ELLIPSYS is parallelized with MPI on distributed memory machines. Notice that ELLIPSYS has been widely used for RANS computations of transitional flows around rotors (Sørensen 2009; Özçakmak *et al.* 2020; Fava *et al.* 2021). Nevertheless, the capabilities of ELLIPSYS for direct numerical or implicit large eddy simulations have not been explored.

2.3. Spatial discretization

The NEK5000 and ELLIPSYS computations are performed with grids with C and O topologies, respectively, as presented in Fig. 1. The number of grid points in the grids is summarized in Table 1. The points listed for the pressure and suction sides correspond to the streamwise direction. In the wake, the points shown are in the streamwise direction in the C grid employed in NEK5000 but in the wall-normal direction in ELLIPSYS due to the O topology. The grid resolution is further assessed by computing $\Delta \xi_{wall}^+ = \Delta \xi_{wall} / (v \sqrt{\tau_w})$, where $\xi = x, y, z$. v is the kinematic viscosity, and τ_w is the wall stress. Δx_{wall}^+ and Δz_{wall}^+ are taken as the maximum over each spectral element in the NEK5000 computations, whereas Δy_{wall}^+ is relative to the height of the first GLL point. The results of this analysis are shown in Fig. 2. The spanwise resolution is very similar in both meshes, as displayed in panel 2a, and remains under 14. The wall-normal resolution in panel 2b is higher in NEK5000 ($\Delta y_{wall}^+ < 0.37$) because the GLL points tend to be clustered near the wall. If one considers the maximum over the element, the values get closer to that from ELLIPSYS. In the streamwise direction, displayed in panel

| Code | Pressure side | Suction side | Trailing edge | Wall-normal direction | Wake | Span |
|----------|---------------|--------------|---------------|-----------------------|------|------|
| ELLIPSYS | 969 | 962 | 120 | 100 | 100 | 160 |
| NEK5000 | 824 | 824 | 208 | 296 | 480 | 160 |

Table 1: Number of grid points.

Figure 2: Wall grid resolution in the spanwise (z), wall-normal (y), and streamwise (x) directions on the suction side (SS, solid lines) and pressure side (PS, dashed lines).

2c, the resolution of ELLIPSYS is generally higher, but $\Delta x_{wall}^+ < 22$ in the NEK5000 results. These values are close to that employed previously in high-fidelity implicit (no-model) LES of airfoils (Tanarro *et al.* 2020; Atzori *et al.* 2020), which proved to yield good agreement with DNS (Negi *et al.* 2018).

3. Effect of the spanwise width of the domain

The computational domain spanwise width L_z is an essential parameter since it will determine what types of structures can be resolved. This is even more pressing in cases where there are laminar separation bubbles and detached flows (Almutairi *et al.* 2010; Eljack & Soria 2020) since the width of the structures forming compares with that of the streamwise dimensions of the LSB. The standard computational domain used by both NEK5000 and ELLIPSYS presents $L_z = 0.1$. The influence of this variable is studied by running a second simulation with NEK5000 using $L_z = 0.2$. This section presents the results of this analysis.

3.1. Perturbation evolution

The streamwise evolution of streamwise velocity perturbations (maximum over the wall-normal direction and spanwise wavenumber β) is studied for selected frequencies, and the

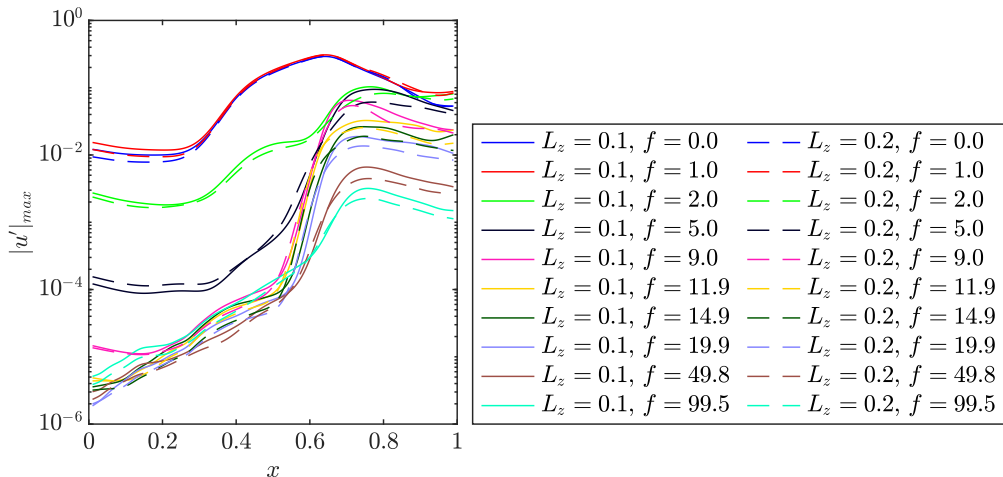
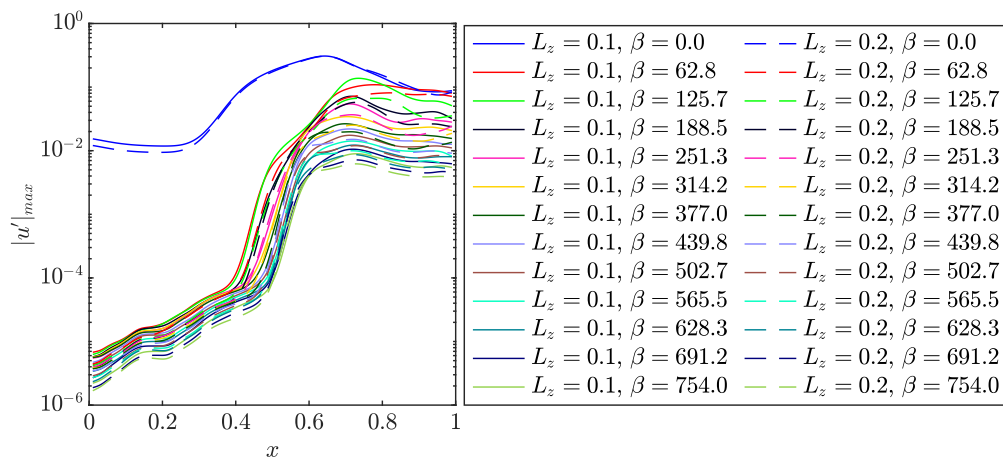
results are presented in Fig. 3a. Steady ($f = 0$) and low-frequency ($f = 1$) perturbations display the highest amplitude. The curves for $L_z = 0.1$ and $L_z = 0.2$ are in close agreement. Furthermore, the agreement improved with the averaging time. Higher-frequency disturbances also display a good matching. Minor disagreements are present in the turbulent flow region towards the end of the domain, but this is expected as very long time series are needed to have converged turbulence statistics. Figure 3b considers the maximum perturbation amplitude over the normal direction and frequency for given β . Two-dimensional ($\beta = 0$) fluctuations present the highest amplitude, with much higher values than three-dimensional disturbances, until the flow becomes turbulent. There is good agreement between the $L_z = 0.2$ and $L_z = 0.1$ curves, although the amplitude for the narrower domain is generally slightly higher. This may be because intermediate spanwise wavenumbers are unresolved in the narrow domain, such as $\beta = 2\pi(2n - 1)/0.2$, with $n = 1, 2, \dots$. Therefore, energy in these modes must be redistributed to the resolved β in the $L_z = 0.1$ simulation, increasing their amplitude. Notice that $\beta = 125.7$ (second spanwise harmonic) presents high amplitude, which even exceeds that of the first harmonic before transition. These modes are related to the spanwise deformation of the flow with the appearance of two spanwise wavelengths in the separation region.

3.2. Instantaneous structures

The instantaneous structures on the suction side of the airfoil for $L_z = 0.1$ and $L_z = 0.2$ are presented in Fig. 4. In panels 4a and 4c, two-dimensional rolls are formed over the laminar separation bubble. These structures correspond to Kelvin-Helmholtz (KH) vortices generated by the roll-up of the shear layer (Dovgal *et al.* 1994). A spanwise modulation of these structures is visible in both cases, more evident in the narrow domain. The analysis of the isosurfaces of w in panels 4b and 4d indicate similar structures for the two domain widths, i.e., in the wider domain, the structure of the $L_z = 0.1$ case appears repeated once more. This further proves that the narrow domain may be sufficient for the computations. Notice that there are two types of structures in these figures. The most upstream one resembles Λ vortices, associated with the secondary instability of Tollmien-Schlichting (TS) waves (Klebanoff *et al.* 1962; Herbert 1988). This instability is present in the front part of the LSB since the KH mode only becomes dominant further downstream, close to the LSB maximum height (Rist & Maucher 2002; Diwan & Ramesh 2009; Jaroslowski *et al.* 2023). Those further downstream structures are farther away from the wall and resemble the three-dimensional breakdown of a shear layer (Rogers & Moser 1992). Furthermore, He *et al.* (2017) found that both short- and long-wavelength (SW and LW) instabilities can occur in these types of transition. Despite the SW instability presenting the highest growth rate, the mode in the current simulations, with only two wavelengths in the spanwise direction for $L_z = 0.1$, is characteristic of an LW mode.

3.3. Time-averaged reverse flow

Figure 5 presents the isosurfaces of time-averaged streamwise velocity for several levels of reverse flow. On the suction side, the flow presents a laminar separation bubble whose initial region is two-dimensional but develops a spanwise modulation further downstream, where the reverse flow is higher. This oscillation is characterized by two spanwise wavelengths in the narrow domain and double in the wide domain. The reattachment line presents a C shape, characteristic of the appearance of a steady global mode that leads to the three-dimensionalization of the reverse flow region (Rodríguez & Theofilis 2009). Such a mode typically requires a minimum reverse flow of -7% (Rodríguez & Theofilis 2010; Rodríguez *et al.* 2013), and the maximum reverse flow on the suction side is much stronger than that,

(a) Maximum over β .(b) Maximum over f .Figure 3: Evolution of streamwise velocity fluctuations (maximum over the normal direction) for narrow ($L_z = 0.1$) and wide ($L_z = 0.2$) domains.

reaching -17%. The flow displays a trailing-edge stall on the pressure side (McCullough & Gault 1951), where the maximum reverse flow is -22%. These values of reverse flow are potentially enough to trigger absolute instability on both sides of the airfoil (Huerre & Monkewitz 1990).

4. Validation of ELLIPSYS for wall-resolved large eddy simulations

Once the narrow domain is shown to be enough for correctly capturing the flow physics, one can proceed with the validation of ELLIPSYS for wall-resolved large eddy simulations (LES), i.e., LES without subgrid-scale model. Validating ELLIPSYS is desirable because of the possibility of running cases with a larger domain and longer time. This is enabled by the ability of ELLIPSYS to deal with non-conformal meshes (now also available in the adaptive

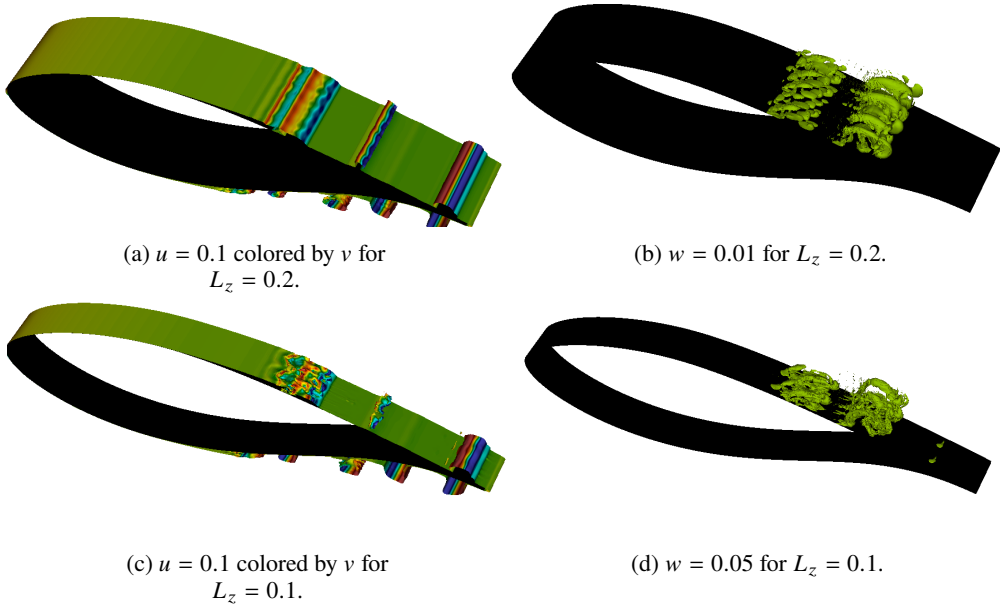


Figure 4: Instantaneous isosurfaces on the suction side of the airfoil for narrow and wide domains at $T = 2.0c/U_\infty$.

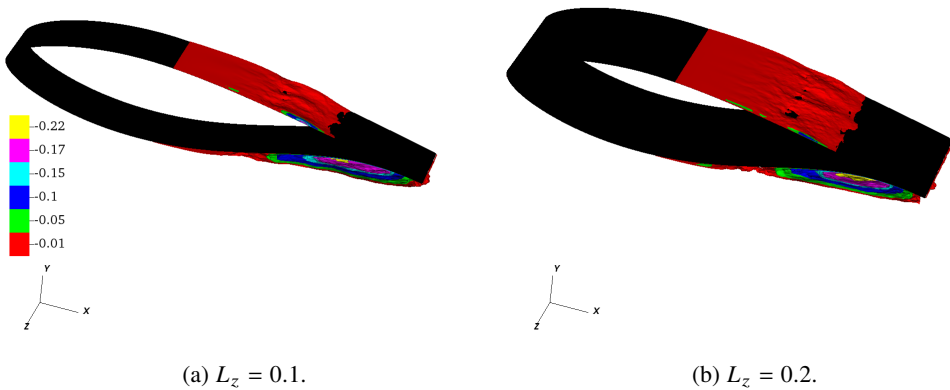


Figure 5: Isosurfaces of time-averaged streamwise velocity for several levels of reverse flow.

mesh refinement implementation of NEK5000 (Offermans 2019)), and a lower order of error truncation, which may be enough for the desired studies of transition.

4.1. Mean flow fields

The pressure coefficient (C_p) obtained with the two solvers is compared in Fig. 6. In general, a good agreement between ELLIPSYS and NEK5000 results is obtained, especially on the suction side of the airfoil (top part of the curves). Certain discrepancies exist between the curves in $x = 0.15 - 0.55$ on the pressure side where NEK5000 predicts a lower pressure. There are

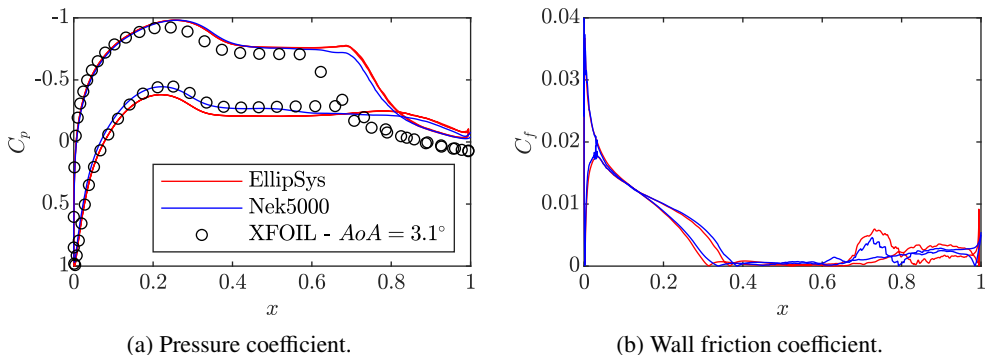


Figure 6: Comparison of pressure and wall-friction coefficients.

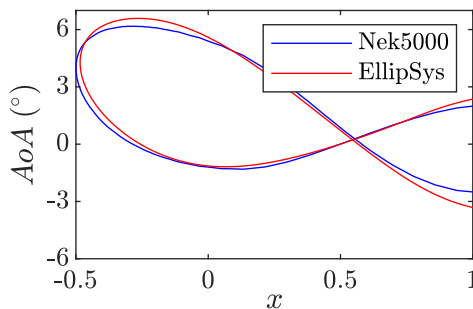


Figure 7: Comparison of the incidence angle on the domain boundaries.

two primary sources for the differences between the codes. The first is the averaging time that is reduced in NEK5000 since the computational cost is much higher than that for running ELLIPSYS. The second is the slightly smaller computational domain in ELLIPSYS, which may constrain the induced velocity, reducing the downwash and leading to a slightly higher effective angle of attack. The variation in the incidence angle on the domain boundaries is compared in Fig. 7, where it is clear that the AoA in ELLIPSYS is slightly higher. This difference is low on the leading-edge plane, in the range $0.06^\circ - 0.2^\circ$ or $3.7\% - 5.3\%$. The effective angle of attack in the simulations, which is typically different from the boundary conditions, is estimated by finding the AoA for which XFOIL (Drela 1989) predicts the closest pressure distribution to that from NEK5000 and ELLIPSYS. An effective $AoA = 3.1^\circ$ is obtained from this analysis for NEK5000, as shown in Fig. 6. The corresponding value for ELLIPSYS is slightly higher, $AoA = 3.3^\circ$. Notice that XFOIL mispredicts C_p in the region with thick separated shear layers. Regarding the wall-friction coefficient (C_f) in Fig. 6b, there is good agreement between NEK5000 and ELLIPSYS until transition occurs, characterized by the increase in C_f at $x = 0.65$.

The spanwise- and time-averaged flow around the airfoil is depicted in Fig. 8 for the horizontal (\bar{U}) and vertical (\bar{V}) velocities. Overall, good agreement is obtained for both components, especially in the front part of the airfoil. Discrepancies occur in the laminar separation bubble (LSB) on the suction side and trailing-edge separation region on the pressure side, where ELLIPSYS predicts a higher reverse flow and thicker shear layer. The over-speed region on the suction side is slightly smaller than that in NEK5000 due to the lower effective AoA .

A more accurate comparison between the near-wall velocity on the suction side is carried

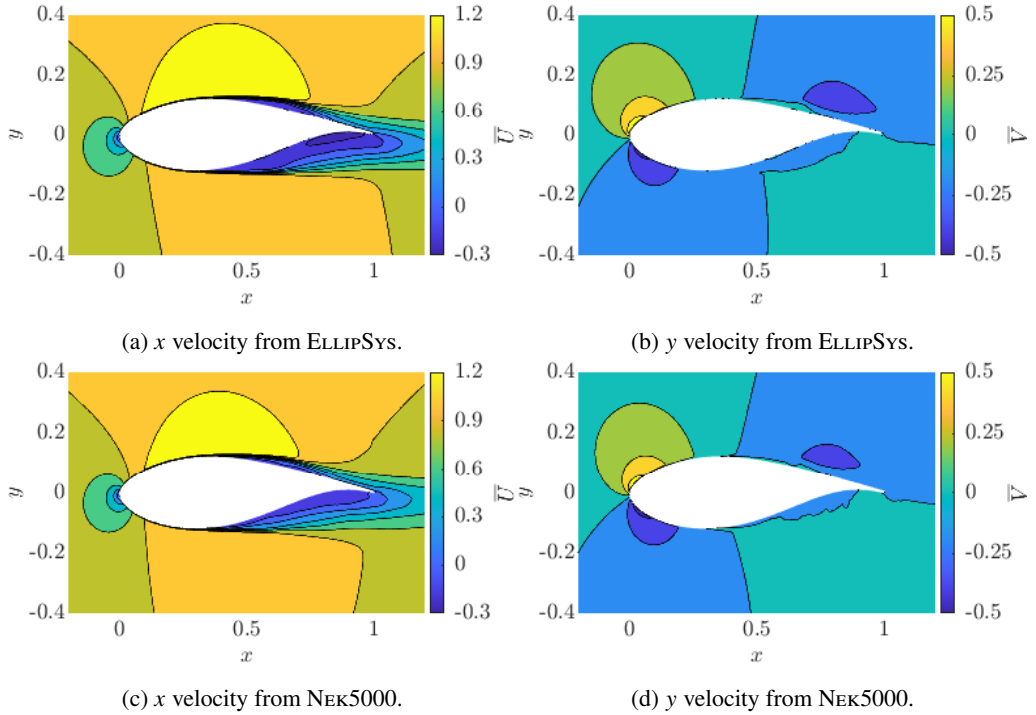


Figure 8: Comparison of the spanwise- and time-averaged horizontal (\bar{U}) and vertical (\bar{V}) velocities in the near field of the airfoil.

out in Fig. 9, where the spanwise- and time-averaged wall-normal profiles of streamwise (\bar{U}) and wall-normal (\bar{V}) velocities from NEK5000 and ELLIPSYS are displayed. Close agreement is obtained for \bar{U} , where only minor differences are observed in the maximum reverse flow at $x = 0.6$. The velocity profiles of \bar{V} are also in close agreement for $x \leq 0.6$, with differences only apparent in the reattached turbulent boundary layer. The agreement improved with the averaging time, indicating that a longer collection of statistics would further reduce the discrepancies. As expected, the results on the pressure side display large differences in the separated shear layer region, which, as discussed above, may be more affected by the slightly lower effective angle of attack in NEK5000.

Table 2 displays the comparison of mean locations of separation (x_{b_1}), reattachment (x_{b_2}), and transition (x_{tr}). The LSB edge is defined as (x, y_b) fulfilling $\int_0^{y_b} \langle U \rangle_{z,t}(x, \xi) d\xi = 0$ (Avanci *et al.* 2019), i.e., y_b is the zero streamwise mass-flux line. The transition location is assumed to be the streamwise locus of maximum boundary layer shape factor $H = \delta^*/\theta$, where δ^* is the displacement thickness and θ is the momentum thickness (Jaroslowski *et al.* 2023). On the suction side, separation starts at $x_{b_1} = 0.374 - 0.381$, and the percentual difference between ELLIPSYS and NEK5000 $\Delta = -1.837\%$ is small. The same is valid for the reattachment point $x_{b_2} = 0.801 - 0.802$, whose difference $\Delta = 0.125\%$ is even lower. A larger discrepancy between the methods occurs for the transition location, which is 6.811% more downstream in ELLIPSYS than in NEK5000. This is likely related to a lower averaging time in NEK5000. On the pressure side, the separation and reattachment locations are in close agreement. Notice that the flow remains separated until the trailing edge. The transition location for ELLIPSYS was estimated as the location of maximum u'_{RMS} since the peak in H

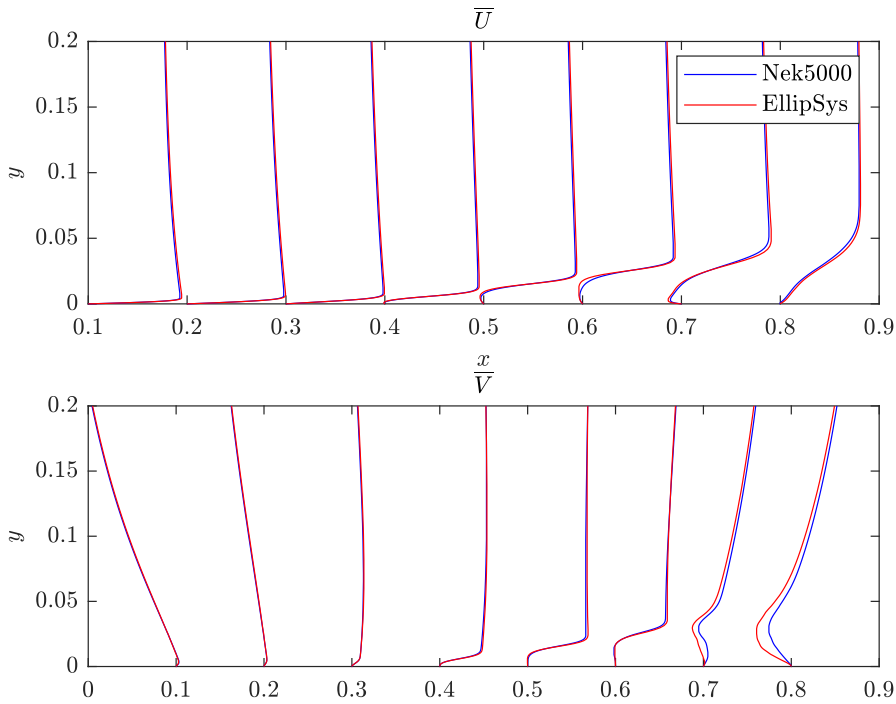


Figure 9: Comparison of the normal profiles of streamwise and normal velocities on the suction side. A scale of 0.1 corresponds to a velocity of 1.4 in the plot of \bar{U} and 0.2 in the one of \bar{V} .

| Code | Suction side | | | Pressure side | | |
|--------------|--------------|-----------|----------|---------------|-----------|---------------|
| | x_{b_1} | x_{b_2} | x_{tr} | x_{b_1} | x_{b_2} | x_{tr} |
| ELLIPSYS | 0.374 | 0.802 | 0.602 | 0.317 | 0.995 | 0.8^\dagger |
| NEK5000 | 0.381 | 0.801 | 0.561 | 0.319 | 1.000 | 0.8114 |
| Δ (%) | -1.837 | 0.125 | 6.811 | -0.631 | 0.503 | - |

Table 2: Mean laminar separation bubble and transition locations.

was not clear. This yielded $x = 0.8^\dagger$, which is close to the transition location in NEK5000 ($x_{tr} = 0.8114$), obtained from the location of maximum H .

4.2. Perturbation evolution

Figure 11 presents a comparison between the boundary layer spectra on the suction side obtained at a wall-normal height of $y = 5 \times 10^{-3}$ with NEK5000 (red line) and ELLIPSYS (blue line). Streamwise (solid line) and normal (dashed line) velocity perturbations are considered. In the attached laminar boundary layer in the region $x = 0.05 - 0.35$, the spectra present differences around $f = 28$, likely corresponding to Tollmien-Schlichting (TS) waves, in which NEK5000 displays higher perturbation amplitude. Notice that these perturbations are very weak and reach a maximum amplitude $\mathcal{O}(10^{-6})$, being damped by numerical dissipation in ELLIPSYS. Since NEK5000 is a pseudo-spectral code, it exhibits nearly zero dissipation. There is good agreement between the codes in the separated flow region ($x = 0.4 - 0.8$) and

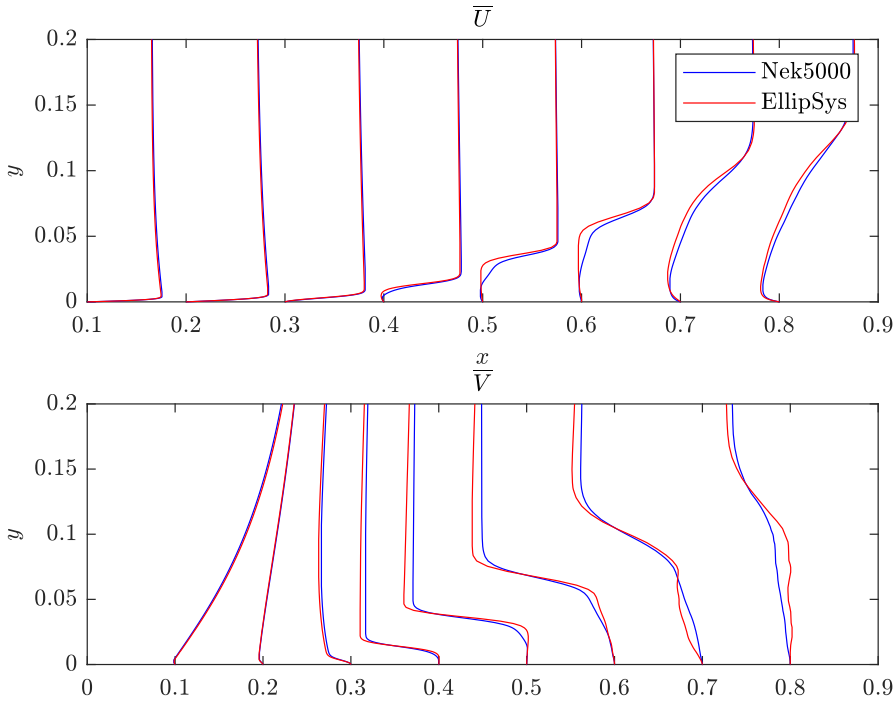


Figure 10: Comparison of the normal profiles of streamwise and normal velocities on the pressure side. A scale of 0.1 corresponds to a velocity of 1.4 in the plot of \bar{U} and 0.2 in the one of \bar{V} .

the reattached turbulent boundary layer ($x > 0.8$). In particular, the energy peak relative to Kelvin-Helmholtz (KH) modes is well captured by both simulations and occurs around $f = 10$ at $x = 0.55$, for example. Regarding the results on the pressure side, shown in Fig. 12, the initial perturbation level ($x = 0.05$), corresponding to numerical noise, is higher in ELLIPSYS, as expected. Further downstream, the perturbation amplitude tends to the same values as boundary-layer instabilities develop. There is an overall good agreement between the results, apart from the peak at $f = 28$ in the attached boundary layer, which is not predicted by ELLIPSYS, similarly to the suction side, due to the higher dissipation in this solver.

4.3. Linear stability analysis

The parabolized stability equations (Bertolotti & Herbert 1991; Bertolotti *et al.* 1992; Herbert 1997) were employed to compute the evolution of convective modes (Huerre & Monkewitz 1990) on the suction side of the blade. These modes consist mainly of TS and KH instabilities. Computations were carried out with the NOLOT PSE code (Hanifi *et al.* 1994). The spanwise- and time-averaged flow was used as base flow for the stability analyses, and only two-dimensional perturbations ($\beta = 0$) were considered as they are the most unstable ones (Squire 1933). Figure 13 shows the N factor, which is a measure of the integrated growth of perturbations, as a function of the temporal frequency and streamwise location. The two neutral curves display good agreement, and the N factor reaches 7.3 for $f = 15$ at the most downstream station analyzed.

Figure 14a presents a comparison between the wall-normal profiles of the $f = 15$, $\beta = 0$ mode (streamwise and wall-normal velocity perturbations) at several streamwise stations

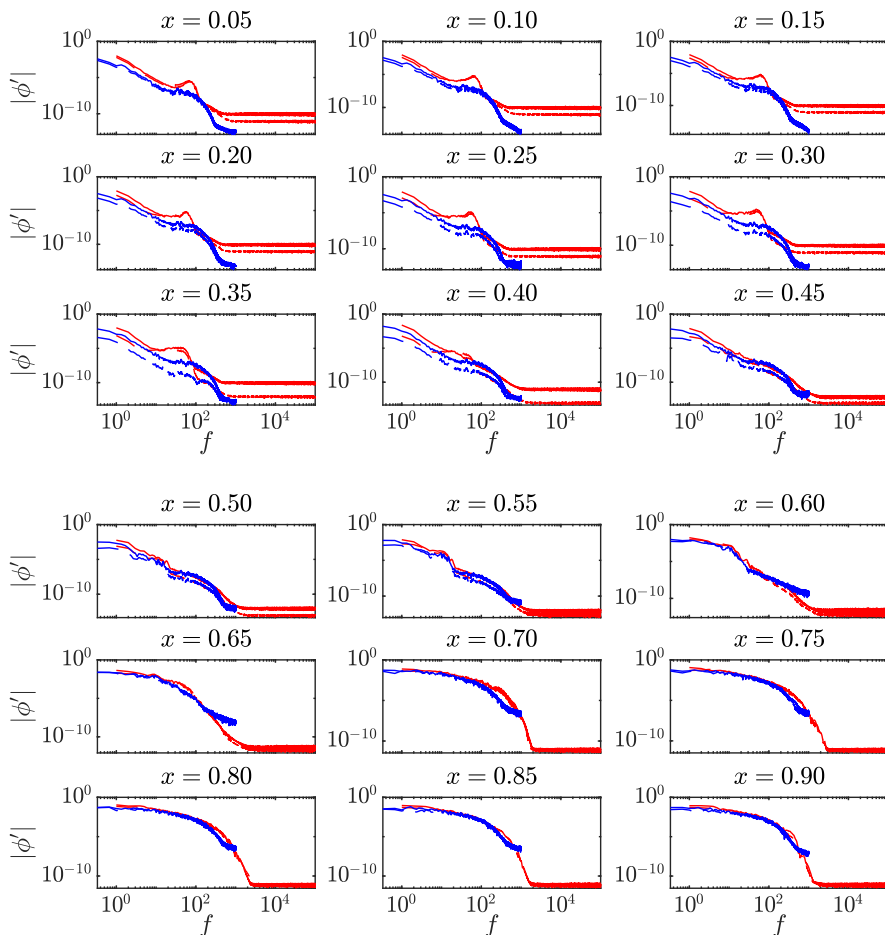


Figure 11: Amplitude spectra of velocity perturbations on the suction side at several streamwise stations. — and - - - indicate streamwise and normal velocity perturbations, respectively, obtained with NEK5000. — and - - - are the corresponding perturbations obtained with ELLIPSYS.

obtained with the mean flows from ELLIPSYS and NEK5000. There is close agreement between the two sets of results for all streamwise positions. It is clear that upstream of separation ($x = 0.3$), the mode corresponds to a TS wave. This changes at the front part of the LSB ($x = 0.4$), where the profile presents a near-wall peak from a TS contribution and a second peak at the inflection point location. The latter peak is characteristic of a KH mechanism, which is inviscid and presents maximum production of perturbation kinetic energy at the inflection point location (Dovgal *et al.* 1994). The TS and KH mechanisms coexist in this region, where the separated shear layer is thin and viscous effects are relevant (Rist 2003; Diwan & Ramesh 2009). Further downstream, at $x = 0.5$, the separated shear layer moves sufficiently far away from the wall so that the inviscid instability becomes the dominant driver of the perturbation kinetic energy production. One can observe that the amplitude at the inflection point location becomes larger than that of the near-wall peak.

The streamwise evolution of the $f = 15$, $\beta = 0$ mode is computed with LES and PSE. The results are presented in Fig. 14b. Despite the higher amplitude in the attached boundary

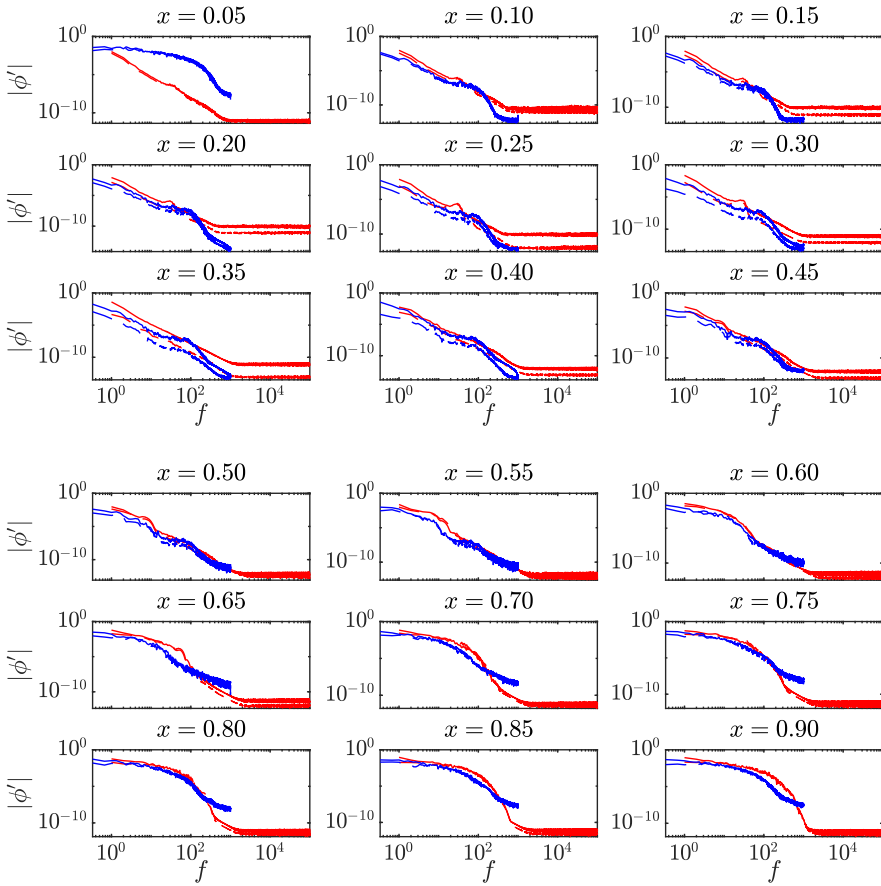


Figure 12: Amplitude spectra of velocity perturbations on the pressure side at several streamwise stations. — and - - - indicate streamwise and normal velocity perturbations, respectively, obtained with Nék5000. — and - - - are the corresponding perturbations obtained with ELLIPSys.

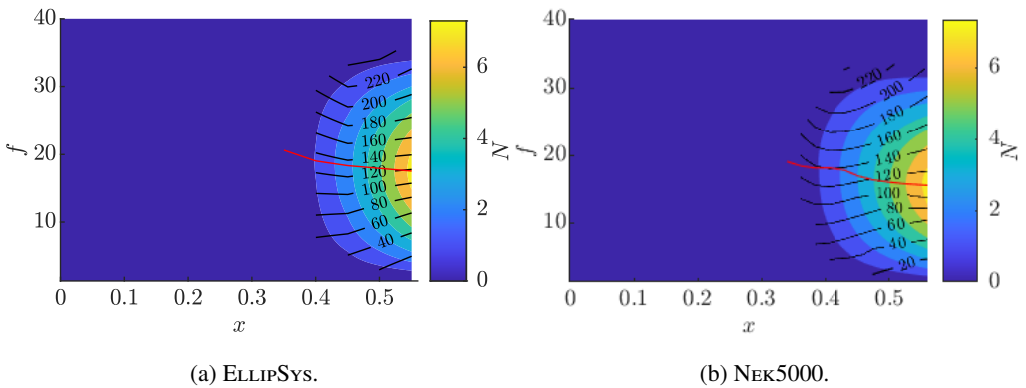


Figure 13: Contours of N factor from PSE. Isolines of the real part of the streamwise wavenumber are show in black. Locus of maximum amplification is highlighted with a red line.

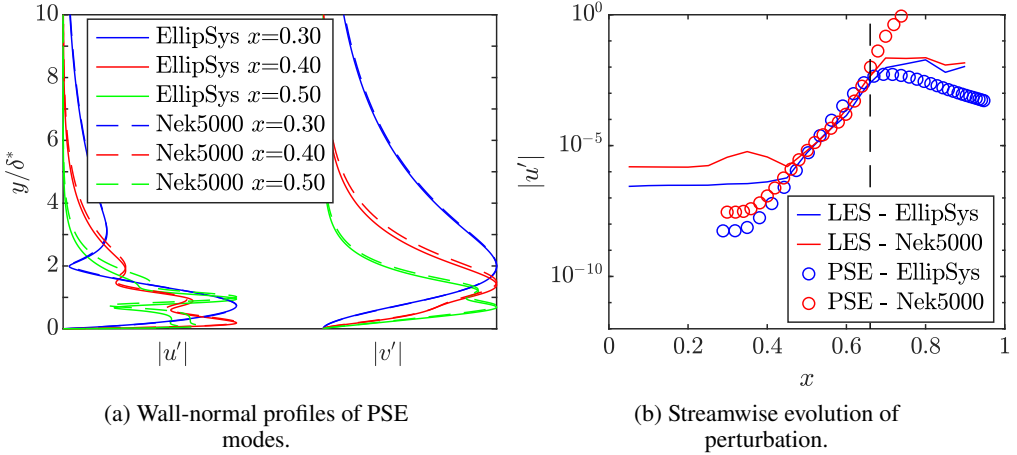


Figure 14: Comparison between PSE and LES computations from NEK5000 and ELLIPSYS for the mode with the highest N factor ($f = 15, \beta = 0$) on the suction side. The vertical line in panel (b) indicates the streamwise location where the perturbation reaches $\mathcal{O}(10^{-2})$.

layer in the NEK5000 results, there is a close agreement for the growth rates computed with this solver and ELLIPSYS in the region where the mode displays the highest growth. This region corresponds to the LSB, where the KH mechanism displays the highest amplification. The agreement remains good along the streamwise extent where non-linear effects are small, which corresponds to the area with perturbation amplitude lower than $\mathcal{O}(10^{-2})$. The location where this occurs is marked with a vertical dashed line. Downstream of that, the mode saturates in the LES simulations, and the mean flow is not representative anymore of the base state where the perturbation grows.

The spatial structure of the $f = 15, \beta = 0$ mode in the LES simulations is investigated with spectral proper orthogonal decomposition (SPOD) (Towne *et al.* 2018; Schmidt & Colonius 2020). This method extracts the most energetic coherent structures, ordering them from the highest (mode 1) to the lowest energy. The analysis domain consists of a region extending from the leading edge to 70% chord on the suction side. 2,000 snapshots spaced with a time step $\Delta t = 5 \times 10^{-3}$ are divided into ten blocks with 80% overlap. The real part of the first SPOD mode for $f = 15, \beta = 0$ is portrayed in Fig. 15, where the streamwise (Ψ_{U_1}) and wall-normal (Ψ_{V_1}) velocity components are presented. The modes agree with previous investigations of the KH instability in LSBs, where $y = \delta^*$ lies approximately at the location of the phase inversion of Ψ_{U_1} and maximum amplitude of Ψ_{V_1} (Fava *et al.* 2023a,b, 2024a).

5. Long-term evolution of the normal force

Once validated, ELLIPSYS is employed to compute the flow development in the long term. The total time of the simulation is $T = 50c/U_\infty$ (50 flowthroughs). In order to remove the transient from the initial condition, the first ten flowthroughs are discarded. The evolution of the normal force coefficient (C_N) as a function of time is presented in Fig. 16. Short-time scales of the order of one flowthrough can be seen in the C_N curve, associated with the shedding of coherent structures from the separated shear layers (Raju *et al.* 2008). In addition, there is a slow modulation of the mean C_N , which may correspond to the phenomenon of low-frequency oscillations (LFOs). The mean variation of the C_N approximately follows a sinusoidal law with angular and temporal frequencies $\omega_f = 0.1309$ and $f_f = 0.021$,

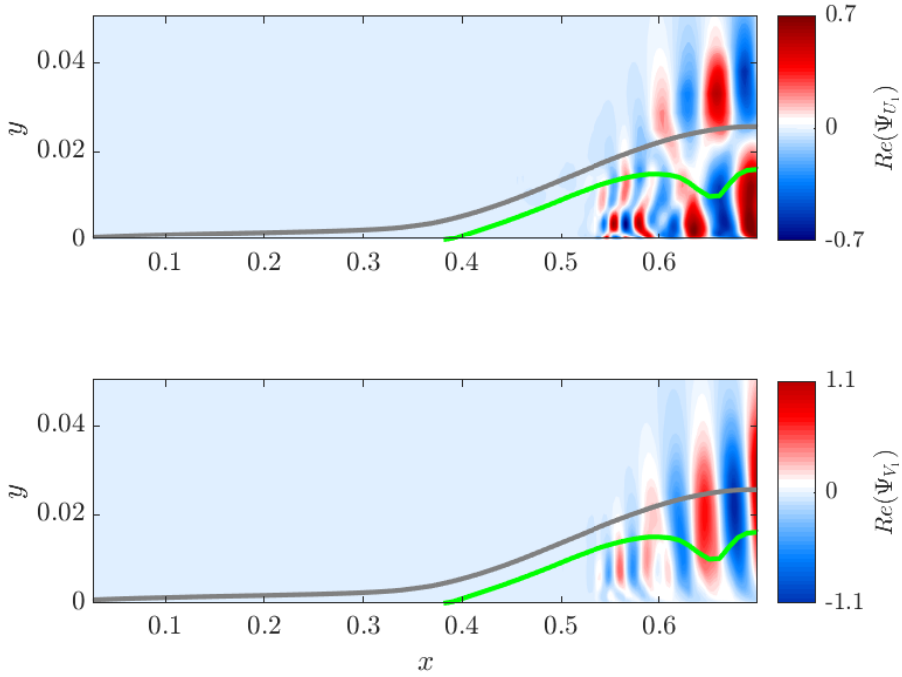


Figure 15: Real part of the first SPOD mode for streamwise and normal velocity perturbations for $f = 15$, $\beta = 0$. The amplitude of the mode corresponds to λ_1 , i.e., the eigenvalue relative to the first mode. The gray line indicates the displacement thickness (δ^*), and the green line denotes the LSB edge (y_b).

respectively, with a corresponding period $T_f = 48$. This frequency is about 720 times lower than the frequency of the most unstable KH mode. Furthermore, this period corresponds to 7.7 rotations of the DTU 10-MW Reference Wind Turbine at rated rotor speed (Bak *et al.* 2012). The widely employed Strouhal number $St = (f^* c / U_\infty) \sin AoA$ (Zaman *et al.* 1987) is computed, yielding $St = 0.0012$, which is in the order of magnitude of LFO in the literature. LFO is attributed to a feedback mechanism between the viscous boundary layer and the inviscid flow, with the alternation between regions of stalled and unstalled flow on the suction side (Zaman *et al.* 1989; Broeren & Bragg 1999; Sandham 2008). The shift from short LSB to fully stalled flow occurs via bursting (McCullough & Gault 1951; Gaster 1967; Aniffa & Mandal 2023). Bursting has been associated with the occurrence of absolute instability (Almutairi & AlQadi 2013; Negi *et al.* 2018), which may happen here due to the reverse flow of -17% (time average) on the suction side (Hammond & Redekopp 1998; Alam & Sandham 2000; Rist & Maucher 2002; Fasel & Postl 2004; Diwan & Ramesh 2009; Rodríguez *et al.* 2013). The amplitude of variation of the C_N in the current case corresponds to approximately 10.5% of its mean value. This is lower than the 50% found in some cases in the literature (Zaman *et al.* 1989; Bernardini *et al.* 2016). A possible explanation for that is that the airfoil is in a post-stall condition.

A compilation of St as a function of the AoA with results from the current work (Fava (2023), FFA-W3) and literature is presented in Fig. 17. Most of the studies were performed for the NACA 0012 and LRN(1)-1007 airfoils, where a well-defined trend of increase in St with AoA exists. Nevertheless, other types of profiles, such as the NACA 643-618 airfoil and NACA 66 hydrofoil, display higher St for the LFO, suggesting that the scaling with St

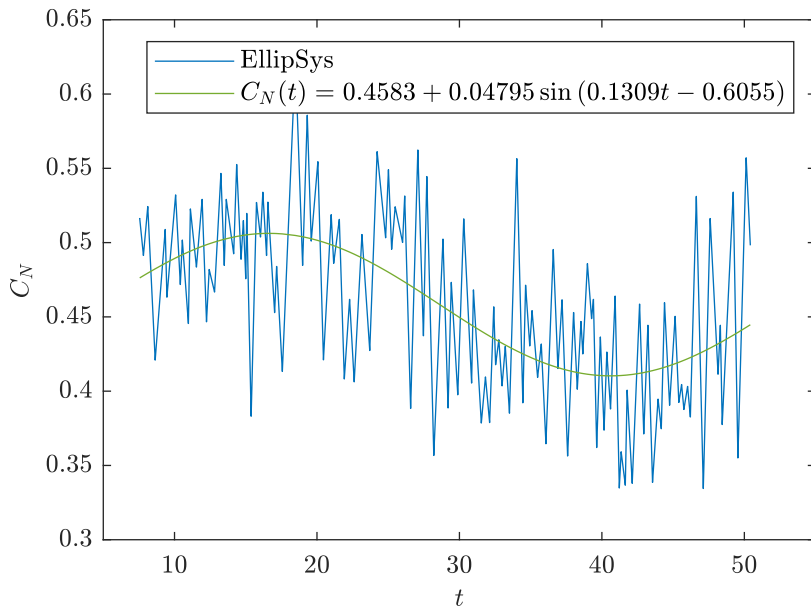


Figure 16: Evolution of the normal force coefficient. SIN is the function $C_N(t) = 0.4583 + 0.04795 \sin(0.1309t - 0.6055)$.

depends on the airfoil geometry. The current work is situated in the bottom left-hand corner of the diagram, with the lowest AoA and St among the results found in the literature. The reason for the appearance of such behavior at low AoA is the thickness of 24% of the current airfoil, which is twice that of the NACA 0012 profile. This leads to stall at relatively low incidence angles (maximum lift at $AoA = 1.4^\circ$ according to XFOIL). Notice, however, that only the pressure side displays a trailing-edge stall in the current simulations. In contrast, the flow reattaches on the suction side, forming an LSB. The figure does not display the dependence of St on the Reynolds number since this variation is small (Bragg *et al.* 1996).

6. Conclusions

The current work studies the transition and low-frequency oscillations (LFOs) phenomena on a wind turbine airfoil. The profile consists of a blend of 96% of the FFA-W3-241 and 4% of the FFA-W3-301 as employed at 68% of the radius of the DTU 10-MW Reference Wind Turbine. Wall-resolved large eddy simulations (LES) of this blade section are conducted with the flow solvers NEK5000 and ELLIPSYS with the chord Reynolds number of 1×10^5 and effective angle of attack of $3.1^\circ - 3.3^\circ$.

The domain width of 10% of the chord was proven enough to capture the flow physics compared to a domain twice wider. Furthermore, ELLIPSYS in LES mode was validated against NEK5000 since the former solver is less computationally demanding. There was close agreement of the mean velocity fields, although small discrepancies were noted in the separated flow region. These minor differences were attributed to the averaging time, limited by NEK5000, and slight variations in the angle of attack. Regarding the perturbation evolution, ELLIPSYS also predicted close results to that from NEK5000, although a peak amplitude in the spectra, corresponding to Tollmien-Schlichting (TS) waves, was underpredicted by ELLIPSYS, probably due to higher numerical dissipation. Transition on the suction side was found to be

| | |
|--------------------------------|--|
| ■ Jones (1993), various | □ Rinoie (2004), NACA 0012 |
| ▲ Farren (1935), RAF 28 x 1.07 | △ Sandham (2008), various |
| ▼ Armstrong (1960), various | ▽ Almutairi (2010), NACA 0012 |
| ▶ Moss (1979), 10C4 | ▷ Almutairi (2013), NACA 0012 |
| ◀ Zaman (1989), LRN(1)-1007 | ◁ Ansell (2015), NACA 0012 |
| ◆ Zaman (1989), NACA 0012 | ◇ Bernardini (2016), NACA 64 ₃ -618 |
| ● Bragg (1993), LRN(1)-1007 | ○ Hristov (2018), NACA 0012 |
| + Heinrich (1994), LRN(1)-1007 | + Liu (2020), NACA 0015 |
| * Bragg (1996), LRN(1)-1007 | * Eljack (2020), NACA 0012 |
| × Broeren (1999), LRN(1)-1007 | × Tang (2021), NACA 66 |
| • Broeren (2000), various | • Eljack (2021), NACA 0012 |
| ★ Gurbacki (2003), NACA 0012 | ☆ Bouchard (2022), OA209 |
| ★ Tanaka (2004), NACA 0012 | ☆ Fava (2023), FFA-W3 |

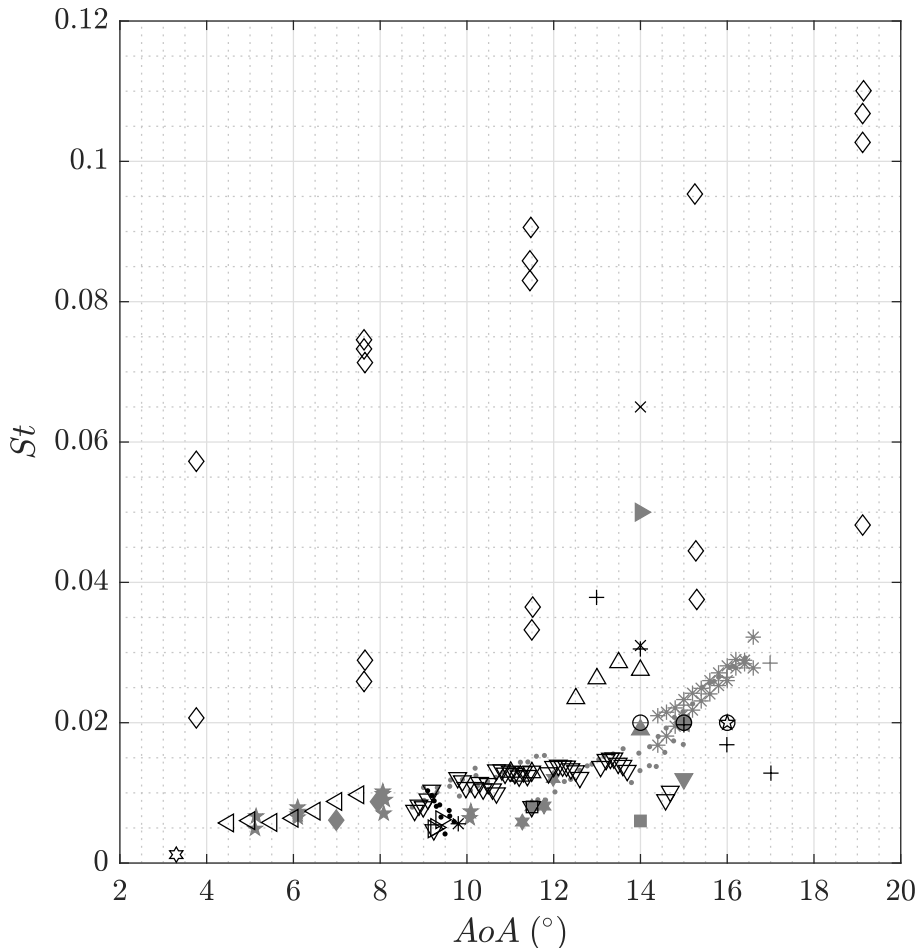


Figure 17: Compilation of $St = (f^*c/U_\infty) \sin AoA$ from the literature and current work (Fava (2023), FFA-W3).

caused by Kelvin-Helmholtz (KH) instability developing on the separated shear layer. The most amplified KH mode presented a frequency $f \approx 15$, with its downstream evolution being closely predicted by the parabolized stability equations (PSE). Furthermore, both solvers indicated very close results.

In the following, ELLIPSYS was employed to compute the long-term evolution of the flow for about 50 flowthroughs. The normal force coefficient (C_N) evolution presented a slow oscillation with an amplitude of 10.5% of the mean and a frequency $f = 0.021$. This converts to $St = (f^*c/U_\infty) \sin \alpha = 0.0012$ for an effective angle of attack of 3.3° . This value of St is in the range of LFO previously observed in airfoils. Nevertheless, from all the compiled results from the literature, the current St is the lowest. The oscillation period corresponds to 7.7 rotations of the DTU 10-MW Reference Wind Turbine at rated rotor speed. These oscillations have been attributed in the literature to the periodic stalling and unstalling of the suction side of the airfoil. The current analysis only noticed a full trailing edge stall on the pressure side, whereas the suction side presented a laminar separation bubble. The reverse flow on both sides was high enough to allow absolute instability, which could explain a periodic bursting of the LSB into fully stalled flow.

REFERENCES

- ALAM, M. & SANDHAM, N. D. 2000 Direct numerical simulation of ‘short’ laminar separation bubbles with turbulent reattachment. *Journal of Fluid Mechanics* **410**, 1–28.
- ALMUTAIRI, JABER H. & ALQADI, IBRAHEEM M. 2013 Large-eddy simulation of natural low-frequency oscillations of separating–reattaching flow near stall conditions. *AIAA Journal* **51** (4), 981–991.
- ALMUTAIRI, JABER H., JONES, LLOYD E. & SANDHAM, NEIL D. 2010 Intermittent bursting of a laminar separation bubble on an airfoil. *AIAA Journal* **48** (2), 414–426.
- ANIFFA, S. M. & MANDAL, A. C. 2023 Experiments on the low-frequency oscillation of a separated shear layer. *Physical Review Fluids* **8** (2), 1–26.
- ANSELL, PHILLIP J. & BRAGG, MICHAEL B. 2015 Characterization of low-frequency oscillations in the flowfield about an iced airfoil. *AIAA Journal* **53** (3), 629–637.
- ARBEY, H. & BATAILLE, J. 1983 Noise generated by airfoil profiles placed in a uniform laminar flow. *Journal of Fluid Mechanics* **134** (1), 33–47.
- ARMSTRONG, E. K. & STEVENSON, R. E. 1960 Some practical aspects of compressor blade vibration. *The Journal of the Royal Aeronautical Society* **64** (591), 117–130.
- ATZORI, MARCO, VINUESA, RICARDO, FAHLAND, GEORG, STROH, ALEXANDER, GATTI, DAVIDE, FROHNAPFEL, BETTINA & SCHLATTER, PHILIPP 2020 Aerodynamic effects of uniform blowing and suction on a naca4412 airfoil. *Flow, Turbulence and Combustion* **105** (3), 735–759.
- AVANCI, MATEUS P., RODRÍGUEZ, DANIEL & ALVES, LEONARDO S. DE B. 2019 A geometrical criterion for absolute instability in separated boundary layers. *Physics of Fluids* **31** (1), 014103.
- BAK, C., BITSCHKE, R. D., YDE, A. & KIM, T. 2012 Light rotor: The 10-mw reference wind turbine. In *Proceedings of EWEA 2012 - European Wind Energy Conference & Exhibition*, pp. 1–10.
- BERNARDINI, CHIARA, BENTON, STUART I., HIPPEL, KYLE D. & BONS, JEFFREY P. 2016 Large low-frequency oscillations initiated by flow control on a poststall airfoil. *AIAA Journal* **54** (5), 1616–1627.
- BERTOLOTTI, F. P. & HERBERT, TH. 1991 Analysis of the linear stability of compressible boundary layers using the pse. *Theoretical and Computational Fluid Dynamics* **3** (2), 117–124.
- BERTOLOTTI, F. P., HERBERT, TH. & SPALART, P. R. 1992 Linear and nonlinear stability of the blasius boundary layer. *Journal of Fluid Mechanics* **242**, 441–474.
- BjÖRCK, A. 1990 Coordinates and calculations for the ffa-w1-xxx, ffa-w2-xxx and ffa-w3-xxx series of airfoils for horizontal axis wind turbines. *Tech. Rep.*. FFA TN 1990-15.
- BOUCHARD, M., MARTY, J., DECK, S. & COSTES, M. 2022 Numerical investigation of self-sustained oscillations of stall cells around a leading edge-separating airfoil. *Physics of Fluids* **34** (11), 115153.
- BRAGG, M. B., HEINRICH, D. C., BALOW, F. A. & ZAMAN, K. B. M. Q. 1996 Flow oscillation over an airfoil near stall. *AIAA Journal* **34** (1), 199–201.
- BRAGG, MICHAEL B., HEINRICH, DOUGLAS C. & KHODADOUST, ABDOLLAH 1993 Low-frequency flow oscillation over airfoils near stall. *AIAA Journal* **31** (7), 1341–1343.

- BRINKERHOFF, JOSHUA R. & YARAS, METIN I. 2011 Interaction of viscous and inviscid instability modes in separation-bubble transition. *Physics of Fluids* **23** (12), 1–11.
- BROEREN, A. P. 2000 An experimental study of unsteady flow over airfoils near stall. PhD thesis, University of Illinois Urbana-Champaign, Urbana, Illinois.
- BROEREN, A. P. & BRAGG, M. B. 1999 Flowfield measurements over an airfoil during natural low-frequency oscillations near stall. *AIAA Journal* **37** (1), 130–132.
- BROEREN, ANDY P. & BRAGG, MICHAEL B. 2001 Spanwise variation in the unsteady stalling flowfields of two-dimensional airfoil models. *AIAA Journal* **39** (9), 1641–1651.
- BROOKS, T. F. & SCHLINKER, R. H. 1983 Progress in rotor broadband noise research. *Vertica* **7** (4), 287–307.
- CERRY, N. J., HILLIER, R. & LATOUR, M. E. M. P. 1984 Unsteady measurements in a separated and reattaching flow. *Journal of Fluid Mechanics* **144**, 13–46.
- CHERUBINI, S., ROBINET, J.-CH. & DE PALMA, P. 2010 The effects of non-normality and nonlinearity of the navier–stokes operator on the dynamics of a large laminar separation bubble. *Physics of Fluids* **22** (1), 014102.
- CORTEN, GUSTAVE P. 2001 Flow separation on wind turbine blades. PhD thesis, Utrecht University, Utrecht.
- CRIMI, P. 1974 Investigation of nonlinear inviscid and viscous flow effects in the analysis of dynamic stall. In *NASA CR-2335*, pp. 1–112. Washington, USA.
- DENG, SHUTIAN, JIANG, LI & LIU, CHAOQUN 2007 Dns for flow separation control around an airfoil by pulsed jets. *Computers & Fluids* **36** (6), 1040–1060.
- DESQUESNES, G., TERRACOL, M. & SAGAUT, P. 2007 Numerical investigation of the tone noise mechanism over laminar airfoils. *Journal of Fluid Mechanics* **591**, 155–182.
- DEVILLE, M. O., FISCHER, P. F. & MUND, E. H. 2002 *High-order methods for incompressible fluid flow*, 1st edn. Cambridge: Cambridge University Press.
- DIWAN, SOURABH S. & RAMESH, O. N. 2009 On the origin of the inflectional instability of a laminar separation bubble. *Journal of Fluid Mechanics* **629**, 263–298.
- DOVGAL, A.V., KOZLOV, V.V. & MICHALKE, A. 1994 Laminar boundary layer separation: instability and associated phenomena. *Progress in Aerospace Sciences* **30** (1), 61–94.
- DRELA, M. 1989 XFOIL: An analysis and design system for low Reynolds number airfoils. In *Lecture Notes in Engineering*, pp. 1–12. Springer Berlin Heidelberg.
- EHRENSTEIN, UWE & GALLAIRE, FRANÇOIS 2008 Two-dimensional global low-frequency oscillations in a separating boundary-layer flow. *Journal of Fluid Mechanics* **614**, 315–327.
- ELJACK, ELTAYEB, SORIA, JULIO, ELAWAD, YASIR & OHTAKE, TOMOHISA 2021 Simulation and characterization of the laminar separation bubble over a naca-0012 airfoil as a function of angle of attack. *Physical Review Fluids* **6** (3), 034701.
- ELJACK, ELTAYEB M. & SORIA, JULIO 2020 Investigation of the low-frequency oscillations in the flowfield about an airfoil. *AIAA Journal* **58** (10), 4271–4286.
- FARREN, W. S. 1935 The reaction on a wing whose angle of incidence is changing rapidly. In *Rep. & M. 1648*. Aeronautics Laboratory, Cambridge.
- FASEL, HERMANN F. & POSTL, DIETER 2004 Interaction of separation and transition in boundary layers: direct numerical simulations. In *Sixth IUTAM Symposium on Laminar-Turbulent Transition* (ed. R. Govindarajan), pp. 71–88. Dordrecht: Springer.
- FAVA, THALES, LOKATT, MIKAELA, SØRENSEN, NIELS, ZAHLE, FREDERIK, HANIFI, ARDESHIR & HENNINGSON, DAN 2021 A simplified model for transition prediction applicable to wind-turbine rotors. *Wind Energy Science* **6** (3), 715–736.
- FAVA, T. C. L., HENNINGSON, D. S. & HANIFI, A. 2024a Boundary layer stability on a rotating wind turbine blade section. *Physics of Fluids* **36** (9), 094128.
- FAVA, T C L, LOBO, B A, NOGUEIRA, P A S, SCHAFFARCZYK, A P, BREUER, M, HENNINGSON, D S & HANIFI, A 2023a Influence of free-stream turbulence on the boundary layer stability of a wind turbine airfoil and near wake. *Journal of Physics: Conference Series* **2505** (1), 012002.
- FAVA, T. C. L., LOBO, B. A., NOGUEIRA, P. A. S., SCHAFFARCZYK, A. P., BREUER, M., HENNINGSON, D. S. & HANIFI, A. 2023b Numerical study of the hydrodynamic stability of a wind-turbine airfoil with a laminar separation bubble under free-stream turbulence. *Physics of Fluids* **35** (8), 1–26.
- FAVA, T. C. L., MASSARO, D., SCHLATTER, P., HENNINGSON, D. S. & HANIFI, A. 2024b Transition to turbulence on a rotating wind turbine blade at $re_c = 3 \times 10^5$. *Journal of Fluid Mechanics* **999**, A54.
- FISCHER, P. F., LOTTES, J. W. & KERKEMEIER, S. G. 2008 Nek5000 web page.
- GASTER, M. 1967 The structure and behavior of laminar separation bubbles. In *Aeronautical Research Council R&M 3595*, pp. 1–31. London.

- GURBACKI, H. M. 2003 Ice-induced unsteady flowfield effects on airfoil performance. PhD thesis, University of Illinois Urbana-Champaign, Champaign, Illinois.
- HAMMOND, D.A. & REDEKOPP, L.G. 1998 Local and global instability properties of separation bubbles. *European Journal of Mechanics - B/Fluids* **17** (2), 145–164.
- HANIFI, A., HENNINGSON, D., HEIN, S., BERTOLOTTI, F. P. & SIMEN, M. 1994 Linear nonlocal instability analysis - the linear nolot code. *Tech. Rep.* FFA TN 1994-54, Bromma, Sweden.
- HE, W., GIORIA, R. S., PÉREZ, J. M. & THEOFILIS, V. 2017 Linear instability of low reynolds number massively separated flow around three naca airfoils. *Journal of Fluid Mechanics* **811**, 701–741.
- HEINRICH, D. C. 1994 An experimental investigation of a low frequency flow oscillation over a low reynolds number airfoil near stall. PhD thesis, University of Illinois Urbana-Champaign, Champaign, Illinois.
- HERBERT, T 1988 Secondary instability of boundary layers. *Annual Review of Fluid Mechanics* **20** (1), 487–526.
- HERBERT, T 1997 Parabolized stability equations. *Annual Review of Fluid Mechanics* **29** (1), 245–283.
- HRISTOV, GEORGI & ANSELL, PHILLIP J. 2018 Poststall hysteresis and flowfield unsteadiness on a naca 0012 airfoil. *AIAA Journal* **56** (7), 2528–2539.
- HUERRE, PATRICK & MONKEWITZ, PETER A. 1990 Local and global instabilities in spatially developing flows. *Annual Review of Fluid Mechanics* **22** (1), 473–537.
- JAROSLAWSKI, TOMEK, FORTE, MAXIME, VERMEERSCH, OLIVIER, MOSCHETTA, JEAN-MARC & GOWREE, ERWIN R. 2023 Disturbance growth in a laminar separation bubble subjected to free-stream turbulence. *Journal of Fluid Mechanics* **956**, 1–33.
- JONES, B. M. 1933 An experimental study of the stalling of wings. In *Aeronautics Research Council R & M 1588*. Aeronautics Laboratory, Cambridge.
- JONES, L. E., SANDBERG, R. D. & SANDHAM, N. D. 2010 Stability and receptivity characteristics of a laminar separation bubble on an aerofoil. *Journal of Fluid Mechanics* **648**, 257–296.
- KLEBANOFF, P. S., TIDSTROM, K. D. & SARGENT, L. M. 1962 The three-dimensional nature of boundary-layer instability. *Journal of Fluid Mechanics* **12** (1), 1–34.
- LIU, JIAN & XIAO, ZHIXIANG 2020 Low-frequency oscillation over naca0015 airfoil near stall at high reynolds number. *AIAA Journal* **58** (1), 53–60.
- MCALPINE, A., NASH, E.C. & LOWSON, M.V. 1999 On the generation of discrete frequency tones by the flow around an aerofoil. *Journal of Sound and Vibration* **222** (5), 753–779.
- MCCULLOUGH, G. B. & GAULT, D. E. 1951 Examples of three representative types of airfoil-section stall at low speed. In *NACA TN-2502*, pp. 1–52. Washington: NACA.
- MICHELSÉN, J.A. 1992 Basis3d - a platform for development of multiblock pde solvers. Technical report AFM 92-05. Technical University of Denmark.
- MICHELSÉN, J.A. 1994 Block structured multigrid solution of 2d and 3d elliptic pde's. Technical Report AFM 94-06. Technical University of Denmark.
- MOSS, N.J. 1979 Measurements of aerofoil unsteady stall properties with acoustic flow control. *Journal of Sound and Vibration* **65** (4), 505–520.
- NASH, EMMA C., LOWSON, MARTIN V. & MCALPINE, ALAN 1999 Boundary-layer instability noise on aerofoils. *Journal of Fluid Mechanics* **382**, 27–61.
- NEGI, P. S., SCHLATTER, P. & HENNINGSON, D. S. 2017 A re-examination of filter-based stabilization for spectral-element methods. *Tech. Rep.* Royal Institute of Technology, Stockholm.
- NEGI, P. S., VINUESA, R., HANIFI, A., SCHLATTER, P. & HENNINGSON, D. S. 2018 Unsteady aerodynamic effects in small-amplitude pitch oscillations of an airfoil. *International Journal of Heat and Fluid Flow* **71**, 378–391.
- OFFERMANS, N. 2019 Aspects of adaptive mesh refinement in the spectral element method. PhD thesis, KTH Royal Institute of Technology, Stockholm.
- ÖZÇAKMAK, ÖZGE SINEM, MADSEN, HELGE AAGAARD, SØRENSEN, NIELS NØRMARK & SØRENSEN, JENS NØRKÆR 2020 Laminar-turbulent transition characteristics of a 3-d wind turbine rotor blade based on experiments and computations. *Wind Energy Science* **5** (4), 1487–1505.
- PASSAGGIA, PIERRE-YVES, LEWEKE, THOMAS & EHRENSTEIN, UWE 2012 Transverse instability and low-frequency flapping in incompressible separated boundary layer flows: an experimental study. *Journal of Fluid Mechanics* **703**, 363–373.
- PATERA, ANTHONY T 1984 A spectral element method for fluid dynamics: Laminar flow in a channel expansion. *Journal of Computational Physics* **54** (3), 468–488.
- PAULEY, LAURA L., MOIN, PARVIZ & REYNOLDS, WILLIAM C. 1990 The structure of two-dimensional separation. *Journal of Fluid Mechanics* **220**, 397–411.

- RAJU, RENI, MITTAL, RAJAT & CATTAFESTA, LOUIS 2008 Dynamics of airfoil separation control using zero-net mass-flux forcing. *AIAA Journal* **46** (12), 3103–3115.
- RINOIE, K. & TAKEMURA, N. 2004 Oscillating behaviour of laminar separation bubble formed on an aerofoil near stall. *The Aeronautical Journal* **108** (1081), 153–163.
- RIST, U. 2003 Instability and transition mechanisms in laminar separation bubbles. In *VKI/RTO-LS Low Reynolds Number Aerodynamics on Aircraft Including Applications in Emerging UAV Technology*, pp. 1–29. Rhode-Saint-Genese, Belgium: von Karman Institute.
- RIST, ULRICH & MAUCHER, ULRICH 2002 Investigations of time-growing instabilities in laminar separation bubbles. *European Journal of Mechanics, B/Fluids* **21** (5), 495–509.
- RODRÍGUEZ, DANIEL, GENNARO, ELMER M. & JUNIPER, MATTHEW P. 2013 The two classes of primary modal instability in laminar separation bubbles. *Journal of Fluid Mechanics* **734** (R4), 1–11.
- RODRIGUEZ, DANIEL & THEOFILIS, VASSILIS 2009 Massively parallel solution of the biglobal eigenvalue problem using dense linear algebra. *AIAA Journal* **47** (10), 2449–2459.
- RODRÍGUEZ, D. & THEOFILIS, V. 2010 Structural changes of laminar separation bubbles induced by global linear instability. *Journal of Fluid Mechanics* **655**, 280–305.
- ROGERS, MICHAEL M. & MOSER, ROBERT D. 1992 The three-dimensional evolution of a plane mixing layer: the kelvin–helmholtz rollup. *Journal of Fluid Mechanics* **243** (1), 183–226.
- SANDHAM, N. D. 2008 Transitional separation bubbles and unsteady aspects of aerofoil stall. *The Aeronautical Journal* **112** (1133), 395–404.
- SCHMIDT, OLIVER T. & COLONIUS, TIM 2020 Guide to spectral proper orthogonal decomposition. *AIAA Journal* **58** (3), 1023–1033.
- SØRENSEN, NIELS N. 2009 Cfd modelling of laminar-turbulent transition for airfoils and rotors using the γ - re_θ model. *Wind Energy* **12** (8), 715–733.
- SQUIRE, HERBERT BRIAN 1933 On the stability for three-dimensional disturbances of viscous fluid flow between parallel walls. *Proceedings of the Royal Society of London. Series A, Containing Papers of a Mathematical and Physical Character* **142** (847), 621–628.
- SØRENSEN, N. N. 1994 General purpose flow solver applied to flow over hills. Technical Report Risø-R-827-(EN). Risø National Laboratory, Roskilde, Denmark.
- TANAKA, H. 2004 Flow visualization and piv measurements of laminar separation bubble oscillating at low frequency on an airfoil near stall. In *Proceedings of the 24th International Congress of the Aeronautical Sciences (ICAS)*, pp. 1–15. Yokohama, Japan.
- TANARRO, ALVARO, MALLOR, FERMÍN, OFFERMANS, NICOLAS, PEPLINSKI, ADAM, VINUESA, RICARDO & SCHLATTER, PHILIPP 2020 Enabling adaptive mesh refinement for spectral-element simulations of turbulence around wing sections. *Flow, Turbulence and Combustion* **105** (2), 415–436.
- TANG, YUAN, WANG, FUJUN, WANG, CHAOYUE, HONG, YIPING, YAO, ZHIFENG & TANG, XUELIN 2021 Low-frequency oscillation characteristics of flow for naca66 hydrofoil under critical stall condition. *Renewable Energy* **172**, 983–997.
- TOWNE, AARON, SCHMIDT, OLIVER T. & COLONIUS, TIM 2018 Spectral proper orthogonal decomposition and its relationship to dynamic mode decomposition and resolvent analysis. *Journal of Fluid Mechanics* **847**, 821–867.
- ZAMAN, K. B. M. Q., BAR-SEVER, A. & MANGALAM, S. M. 1987 Effect of acoustic excitation on the flow over a low-re airfoil. *Journal of Fluid Mechanics* **182** (1), 127–148.
- ZAMAN, K. B. M. Q., MCKENZIE, D. J. & RUMSEY, C. L. 1989 A natural low-frequency oscillation of the flow over an airfoil near stalling conditions. *Journal of Fluid Mechanics* **202**, 403–442.
- ZAMAN, K. B. M. Q. & POTAPCZUK, M. G. 1989 The low-frequency oscillation in the flow over a naca 0012 airfoil with an ‘iced’ leading edge. In *NASA TM-102018*, pp. 1–16.